applied sciences

MDPI

Article

Multiscale Analysis of Anisotropy of Reynolds Stresses, Subgrid Stresses and Dissipation in Statistically Planar Turbulent Premixed Flames

Markus Klein [1], Theresa Trummler [1], Noah Urban [1] and Nilanjan Chakraborty [2,*]

[1] Department of Aerospace Engineering, Bundeswehr University Munich, 85577 Neubiberg, Germany; markus.klein@unibw.de (M.K.); theresa.trummler@unibw.de (T.T.); noah.urban@unibw.de (N.U.)
[2] School of Engineering, Newcastle University, Newcastle NE1 7RU, UK
* Correspondence: nilanjan.chakraborty@newcastle.ac.uk

Abstract: The characterisation of small-scale turbulence has been an active area of research for decades and this includes, particularly, the analysis of small-scale isotropy, as postulated by Kolmogorov. In particular, the question if the dissipation tensor is isotropic or not, and how it is related to the anisotropy of the Reynolds stresses is of particular interest for modelling purposes. While this subject has been extensively studied in the context of isothermal flows, the situation is more complicated in turbulent reacting flows because of heat release. Furthermore, the landscape of Computational Fluid Dynamics is characterised by a multitude of methods ranging from Reynolds-averaged to Large Eddy Simulation techniques, and they address different ranges of scales of the turbulence kinetic energy spectrum. Therefore, a multiscale analysis of the anisotropies of Reynolds stress, dissipation and sub-grid scale tensor has been performed by using a DNS database of statistically planar turbulent premixed flames. Results show that the coupling between dissipation tensor and Reynolds stress tensor is weaker compared to isothermal turbulent boundary layer flows. In particular, for low and moderate turbulence intensities, heat release induces pronounced anisotropies which affect not only fluctuation strengths but also the characteristic size of structures associated with different velocity components.

Keywords: anisotropies of Reynolds stress tensor; dissipation tensor and subgrid scale tensor; multiscale analysis; turbulent premixed flames

check for updates

Citation: Klein, M.; Trummler, T.; Urban, N.; Chakraborty, N. Multiscale Analysis of Anisotropy of Reynolds Stresses, Subgrid Stresses and Dissipation in Statistically Planar Turbulent Premixed Flames. *Appl. Sci.* **2022**, *12*, 2275. https://doi.org/10.3390/app12052275

Academic Editors: Alexey Burluka, Andrei Lipatnikov and N.C. Markatos

Received: 16 January 2022
Accepted: 15 February 2022
Published: 22 February 2022

1. Introduction

Based on the hypothesis that the nonlinear turbulent energy transfer process from large to small scales is accompanied with a loss of directional information, Kolmogorov postulated [1] that small-scale turbulent motions are statistically isotropic [2] at sufficiently high values of Reynolds numbers. In fact, the fundamental argument of the Large Eddy Simulation (LES) approach is that small-scale structures are easier and more universal to model because they are assumed to be isotropic and independent of the flow geometry which only affects energy-carrying eddies. By contrast, in Reynolds-averaged Navier–Stokes-based modelling (RANS), the full range of structures requires modelling, which obviously calls for considerably more complex constitutive equations for closing Reynolds stresses. For sufficiently high Reynolds numbers, there is a distinct scale separation between the energy spectrum (dominant at larger scales) and the dissipation spectrum (dominant at the smallest scales of motion), and it is often assumed that the dissipation tensor $\varepsilon_{ij} = 2\langle \nu\, \partial u_i'/\partial x_k\, \partial u_j'/\partial x_k \rangle$ (with ν being the kinematic viscosity) obeys an isotropic relation of the form $\varepsilon_{ij} = \varepsilon\delta_{ij}/3$, while the anisotropies of the Reynolds stresses $\langle u_i' u_j' \rangle$, where angled brackets denote a suitable averaging operation, are conveniently characterised with the help of the anisotropy tensor a_{ij} given by the following equation:

$$a_{ij} = \frac{\langle u_i' u_j' \rangle}{2k} - \frac{1}{3}\delta_{ij} \quad k = \frac{1}{2}\langle u_i' u_j' \rangle \tag{1}$$

where k is the turbulence kinetic energy. It is noted that the anisotropy of the dissipation tensor e_{ij} can be defined by the same analogy. Instead of an isotropic relation $\varepsilon_{ij} = \varepsilon\delta_{ij}/3$, a linear relation between the dissipation tensor and the Reynolds stress anisotropy has been suggested by Hanjalic and Launder [3]. Antonia et al. [4] suggested a linear relationship between the dissipation tensor and the anisotropy tensor with a Reynolds number dependent constant of proportionality. By contrast, Liu and Pletcher [5] proposed an anisotropic model, which approximates anisotropy tensor a_{ij} by a normalised turbulent dissipation tensor. It becomes clear from the foregoing discussion that the relationship between Reynolds stress tensor and dissipation tensor plays a fundamental role in RANS based turbulence modelling, a topic reviewed in the 1990s by Launder [6] and Speziale [7] or more recently in a variety of textbooks [2,8–10].

Apart from the modelling aspect, the physics of small-scale turbulence, which is strongly associated with the mechanism of dissipation, has been an active area of research for several decades (e.g., Sreenivasan and Antonia [11]). Shen and Warhaft [12] reported, for turbulent shear flows up to a Taylor scale Reynolds number of $Re_\lambda = 1000$, that the postulate of local isotropy is untenable, both at dissipation and inertial scales, and they suggested that it is unlikely to be so even at higher Reynolds numbers. The multiscale behaviour of anisotropy occurring in turbulent boundary layers has been analysed by Liu and Pletcher [5], who reported that anisotropy does not decay as scales decrease.

In turbulent premixed combustion, the situation can become even more complicated due to the anisotropic nature of heat release. This is closely related to the phenomenon of counter-gradient transport, which has been theoretically explained by Clavin and Williams [13] and Libby and Bray [14] and has been observed in many experimental and numerical studies, as reviewed in Klein et al. [15,16] and Brearley et al. [17], where combustion-induced flow anisotropy has been characterised with the help of the so-called Lumley triangle [18]. However, the relation between Reynolds stress tensor and dissipation tensor anisotropies has, to the best knowledge of the authors, not been explored in the context of turbulent premixed combustion. As the landscape of Computational Fluid Dynamics (CFD) methods is full of different modeling approaches ranging from classical RANS models to hybrid RANS-LES to LES methods, it will be of particular interest to perform a multiscale analysis of turbulence anisotropies which reflects the nature of the associated different unclosed terms. In this regard, the main objectives of this study are the following: (i) perform a multiscale analysis of the anisotropies of Reynolds stress, dissipation and subgrid scale tensors for a large range of different filter sizes, (ii) to compare their level of anisotropy for different turbulence intensities and (iii) to provide detailed physical explanations for the observed behaviour.

The rest of the paper is organised as follows: Section 2 introduces the database and the numerical methods and Section 3 provides the mathematical framework for the subsequent analysis. Results will be presented in Section 4 and the main findings will be summarised in Conclusions.

2. Numerical Methodology and DNS Database

Three turbulent, statistically planar premixed flames with global Lewis number $Le = 1.0$, representing stoichiometric methane-air flames preheated to 415 K, have been chosen from a larger database that has been described in [19,20]. The compressible Navier–Stokes equations have been solved in nondimensional form (see, e.g., [21]) using the well-known SENGA code [22]. As this work focuses on the fluid dynamical aspects of reacting flows, a generic single step Arrhenius type irreversible chemistry has been employed, which provides the same qualitative and very similar quantitative behaviour of flame turbulence interaction [23] compared to a detailed chemical mechanism, in particular, with respect to flow anisotropy [15,16].

The turbulence Reynolds number Re_t, normalised turbulent root-mean-square (rms) velocity fluctuation u'/S_L, integral length scale to thermal flame thickness ratio l/δ_{th}, Damköhler number Da and Karlovitz number Ka for cases A–C are shown in Table 1. The definitions of these quantities are given as follows.

$$Da = \frac{lS_L}{\delta_{th}u'} Ka = \left(\frac{u'}{S_L}\right)^{\frac{3}{2}} \left(\frac{l}{\delta_{th}}\right)^{-\frac{1}{2}} \delta_{th} = \frac{T_{ad} - T_0}{\max|\nabla T|_L} \tau = \frac{T_{ad} - T_0}{T_0} \beta = \frac{T_{ac}(T_{ad} - T_0)}{T_{ad}^2} \quad (2)$$

Here, δ_{th} is the thermal flame thickness, and S_L (with the subscript L referring to unstrained laminar flame quantities) is the laminar burning velocity. The heat release parameter τ (with the adiabatic and fresh gas temperatures T_{ad}, T_0) and the Zel'dovich number β (T_{ac} is the activation temperature) are 4.5 and 6.0, respectively, for the stoichiometric methane–air flames preheated to 415 K. Standard values of Prandtl number ($Pr = 0.7$) and ratio of specific heats ($\gamma = 1.4$) have been used, which are consistent with unity Lewis number assumption.

Table 1. Initial parameters for the three turbulent premixed flames considered in this analysis.

Case	Re_t	u'/S_L	l/δ_{th}	Da	Ka
A	11.67	1.0	4.58	4.58	0.47
B	87.5	7.5	4.58	0.61	9.6
C	175.0	15.0	4.58	0.31	27.16

Flame–turbulence interaction takes place under decaying turbulence, and the values reported in Table 1 have to be understood as initial values. The simulation time is taken to be the chemical time scale $t_{chem} = \delta_{th}/S_L$, which is in all cases larger than the eddy turnover time $t_{EDT} = l/u'$. Advantages and disadvantages of this particular setup have been discussed in detail in [24], and it has been checked that the results are qualitatively similar to those obtained from a database with unburned gas forcing [25], which are not explicitly shown here for the sake of brevity. While the decaying turbulence setup potentially has a history effect, it is not important for the qualitative nature of the results presented in this work. This approach ensures that flame development is mostly natural and possible artificial effects due to the forcing term in the Navier–Stokes equations can be avoided. While the reacting flow and species fields are initialised by a steady planar unstrained premixed laminar flame solution, turbulent velocity fluctuations are initialised using a homogeneous isotropic incompressible velocity field in conjunction with a model spectrum suggested by Pope [2]. The simulation domain is taken to be a cube with side length $26.1\delta_{th}$, which is discretised using a uniform Cartesian grid of dimension 512^3. This ensures sufficient resolution of the flame structure (11 grid points are kept within δ_{th}) and the smallest scales in the turbulent flow. It has been found that coarsening the mesh by factor of 2.0 did not make any significant influence on the values of S_L and δ_{th} (<1% change); thus, the grid spacing considered here deemed appropriate for the current analysis. The timestep has been determined by the acoustic CFL criterion and it remained at about 0.1 for all computations reported in this paper. An increase in CFL number by a factor 2.0 did not significantly affect the values of S_L and δ_{th} (i.e., less than 0.1% difference). Time integration is performed using an explicit third-order low-storage Runge–Kutta scheme, and spatial derivatives for all internal grid points are evaluated using a 10th order central difference scheme, but the order of accuracy gradually drops to a one-sided second-order scheme at the non-periodic boundaries. The SENGA code is well established in the scientific community, and its implementation has been verified several times in the past. Exemplarily, it is mentioned that for a Taylor–Green vortex, the maximum deviation in enstrophy with respect to reference data [26,27] is 2.5%, while kinetic energy can be considered to be identical with those reference solutions. The boundary conditions in the mean flame propagation direction are taken to be partially nonreflecting, whereas boundaries in transverse directions are taken to be periodic. The computational cost is of the order of 10^5 CPU hours (on Intel Xeon E5) for each of the cases considered here.

Figures 1–3 show the instantaneous distribution of reaction progress variable c with superimposed isocontours corresponding to $c = 0.1,\ 0.5,\ 0.9$ for cases A–C in two different sections cutting the computational domain in x-y and y-z direction. In all figures, the flame propagates from right to left along the negative x-direction. In this context, the reaction progress variable c is defined based on the reactant mass fraction Y_R as follows: $c = (Y_{R0} - Y_R)/(Y_{R0} - Y_{R\infty})$ where the subscripts 0 and ∞ refer to the values in the unburned reactants and fully burned products, respectively. It can be observed from Figure 1 that c-isosurfaces are mostly parallel to each other in case A, whereas the $c = 0.1$ isosurface is more distorted than the $c = 0.9$ in cases B and C. The Karlovitz number increases from case A to case C (see Table 1), which results in a larger length scale separation between δ_{th} and η. As a consequence, energetic turbulent eddies are more likely to perturb the preheat zone for high values of Ka and local flame thickening can be observed in case C. Furthermore, it can be also observed from Figures 1–3 that flame wrinkling increases from case A to case C. While turbulent structures tend to be relatively isotropic for cases B and C, case A clearly shows larger structures for the velocity fluctuations which are aligned with the mean flame propagation direction (i.e. u'/S_L) compared to those which are normal to the x-direction (e.g., v'/S_L).

Bray et al. [28] derived the following expression of $\langle \rho u_i'' u_j'' \rangle$ based on a presumed bi-modal probability density function (PDF) of reaction progress variable c.

$$\begin{aligned}\langle \rho u_i'' u_j'' \rangle = \langle \rho \rangle \{c\} \quad & (1 - \{c\})[\langle u_i \rangle_P - \langle u_i \rangle_R]\left[\langle u_j \rangle_P - \langle u_j \rangle_R\right] \\ & + \langle \rho \rangle (1 - \{c\}) \langle u_i' u_j \rangle_R + \langle \rho \rangle \{c\} \langle u_i' u_j \rangle_P + O(\gamma_c)\end{aligned} \tag{3}$$

Here, $\{Q\}$ is the Favre-averaged/filtered value of a quantity Q, defined as $\{Q\} = \langle \rho Q \rangle / \langle \rho \rangle$ and the corresponding Favre fluctuation is given by $Q'' = Q - \{Q\}$. The quantities $\langle Q \rangle_R$ and $\langle Q \rangle_P$ refer the averaged/filtered values of Q conditioned upon reactants and products, respectively. The first term on the right-hand side of Equation (3) accounts for the effects of thermal expansion arising from heat release, whereas the second and third terms arise due to non-reacting turbulence effects and the last term on the right-hand side of Equation (3) originates from the interior of the flame. The last term on the right-hand side of Equation (3) remains small in magnitude for $Da \gg 1$ under which the PDF of c can be considered to be bimodal. Whether the PDF of c is bimodal for the cases considered here is not relevant for the discussion in this paper, and Equation (3) provides important physical insights into the qualitative behaviour of $\langle \rho u_i'' u_j'' \rangle$ irrespective of the validity of the bimodality of the c-PDF. Veynante et al. [29] demonstrated that slip velocity $[\langle u_i \rangle_P - \langle u_i \rangle_R]$ can be expressed as follows:

$$[\langle u_i \rangle_P - \langle u_i \rangle_R] = -\left(\alpha_E u' + \tau S_L\right) M_i \tag{4}$$

where $M_i = -(\partial \widetilde{c}/\partial x_i)/|\nabla \widetilde{c}|$ is i^{th} component of the normal vector based on the flame brush and α_E is a model parameter of the order of unity. Based on Equation (4), Veynante et al. [28] defined a nondimensional parameter known as the Bray number $NB \sim \tau S_L/u' \sim \tau/\left(Da^{1/2} Ka\right)$ to decide if the velocity jump across the flame brush due to heat release is greater ($NB > 1$) or smaller ($NB < 1$) than the turbulent velocity fluctuations. For cases A–C, the Bray number is given by 4.5, 0.6 and 0.3, respectively, based on the initial conditions, which shows that the Reynolds stresses in case A are likely to be dominated by effects of heat release, whereas cases B and C are increasingly influenced by turbulent velocity fluctuations. By contrast, the large-scale strain rate a_{turb} in the context of RANS can be scaled as u'/l [30], whereas the strain rate induced by thermal expansion a_{chem} can be scaled as $\tau S_L/\delta_{th}$ [31]. Therefore, the ratio of the strain rates induced by thermal expansion due to heat release to the large-scale turbulent strain rate can be scaled as $a_{chem}/a_{turb} \sim \tau Da$ [31]. The values of Da in Table 1 reveal that the influence of a_{chem} is likely to progressively weaken in comparison to the effects of a_{turb} from case A to case C. Thus, the statistics of ε_{ij} in case A are likely to be strongly influenced by heat release, whereas these statistics are expected to be influenced by turbulent straining in case C. The relative strength of thermal expansion in comparison to the background flow turbulence will affect the flow anisotropies as discussed in Section 4.

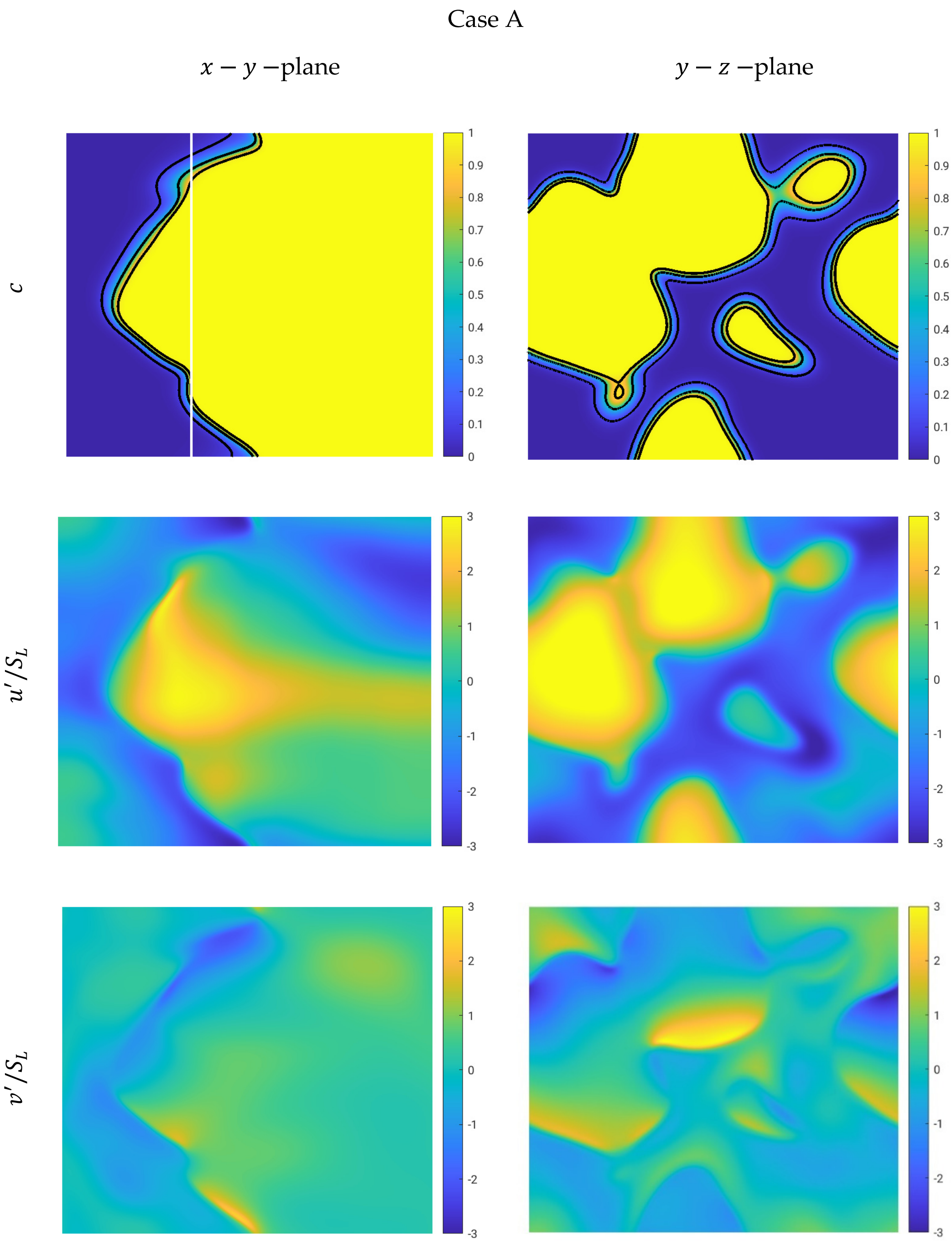

Figure 1. Top: Instantaneous distribution of reaction progress variable with superimposed isocontours corresponding to $c = 0.1,\ 0.5,\ 0.9$. The white line shows the position of the mean flame brush corresponding to $\bar{c} = 0.5$, which demarks the position of the y-z plane. Middle and bottom: Instantaneous, normalised velocity fluctuations in direction aligned with (u'/S_L) and normal to (v'/S_L) mean flame propagation direction. Results are shown for case A in the x-y (**left**) and y-z plane (**right**). The flame propagates from right to left along the negative x-direction. The field of view represents the computational domain of dimension $26.1\delta_{th} \times 26.1\delta_{th}$.

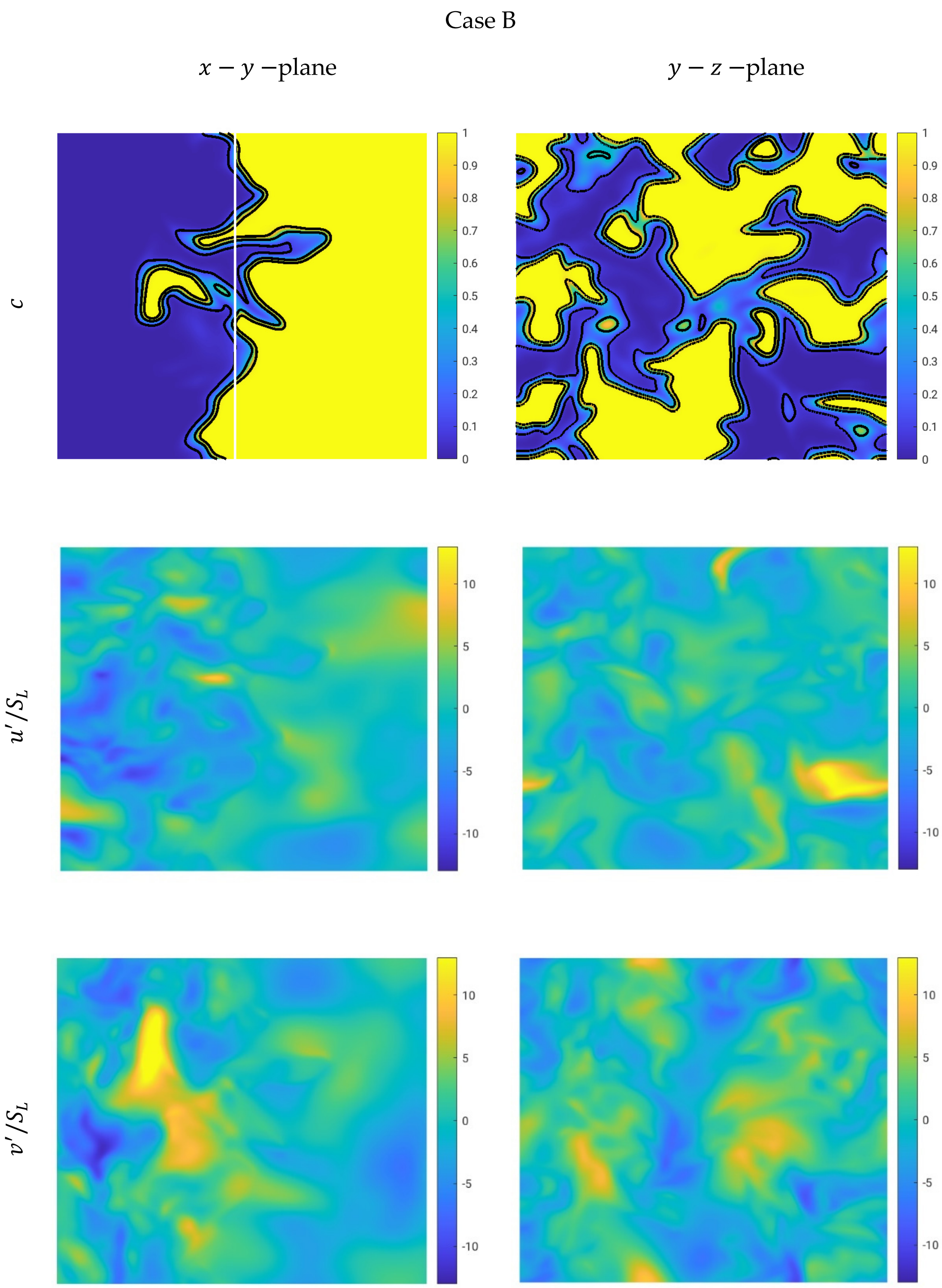

Figure 2. Top: Instantaneous distribution of reaction progress variable with superimposed isocontours corresponding to $c = 0.1,\ 0.5,\ 0.9$. The white line shows the position of the mean flame brush corresponding to $\bar{c} = 0.5$, which demarks the position of the y-z plane. Middle and bottom: Instantaneous, normalised velocity fluctuations in direction aligned with (u'/S_L) and normal to (v'/S_L) mean flame propagation direction. Results are shown for case B in the x-y (**left**) and y-z plane (**right**). The flame propagates from right to left along the negative x-direction. The field of view represents the computational domain of dimension $26.1\delta_{th} \times 26.1\delta_{th}$.

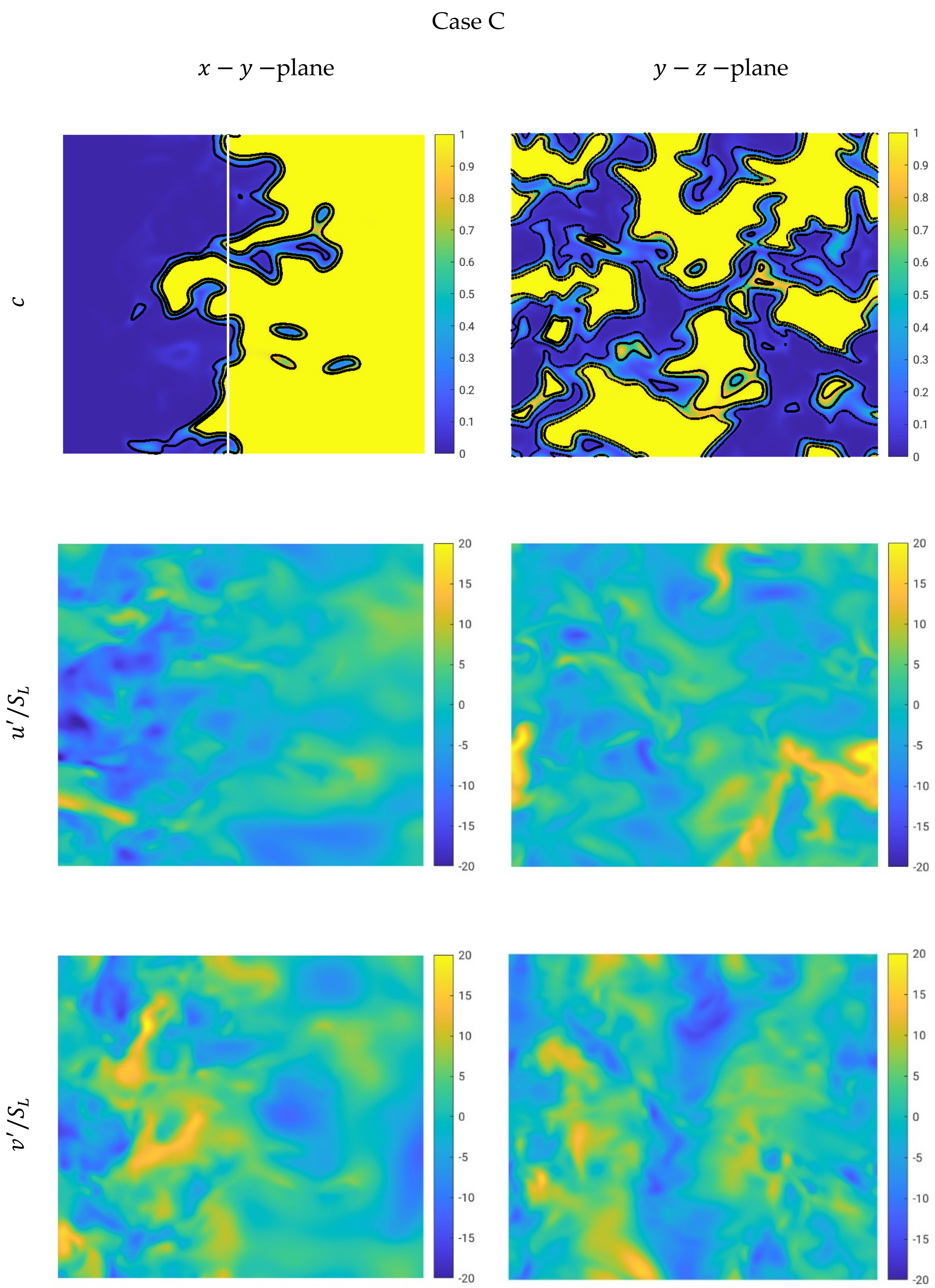

Figure 3. Top: Instantaneous distribution of reaction progress variable with superimposed isocontours corresponding to $c = 0.1,\ 0.5,\ 0.9$. The white line shows the position of the mean flame brush corresponding to $\bar{c} = 0.5$, which demarks the position of the y-z plane. Middle and bottom: Instantaneous, normalised velocity fluctuations in direction aligned with (u'/S_L) and normal to (v'/S_L) mean flame propagation direction. Results are shown for case C in the x-y (**left**) and y-z plane (**right**). The flame propagates from right to left along the negative x-direction. The field of view represents the computational domain of dimension $26.1\delta_{th} \times 26.1\delta_{th}$.

3. Mathematical Background

The turbulent state and its anisotropy can be analysed in the so-called Lumley triangle [18]. The boundaries of the triangle are defined in terms of the second II_a and third III_a invariant of the tensor a_{ij} (and by analogy for e_{ij}) after introducing variables η and ξ in the following manner.

$$II_a = \frac{trace(a)^2 - trace(a^2)}{2},\ III_a = \det(a),\ \eta = \left(-\frac{1}{3}II_a\right)^{1/2},\ \xi = \left(\frac{1}{2}III_a\right)^{1/3} \quad (5)$$

Two borders are given by the straight lines connecting the origin (0,0) with the points $(-1/6, 1/6)$ and $(1/3, 1/3)$, respectively, while $\eta = \left(1/27 + 2\xi^3\right)^{1/2}$ represents the third, curved border. Any physically realizable state of the anisotropy tensors has to lie within this triangle and the borders, sketched in Figure 4a, represent an axisymmetric contraction (left border), axisymmetric expansion (right border) and the two-component state, respectively, while the origin demarks the isotropic state [2]. Coordinates ξ and η are nondimensional quantities; thus, the Lumley triangle provides a general framework for the parameterization of anisotropy.

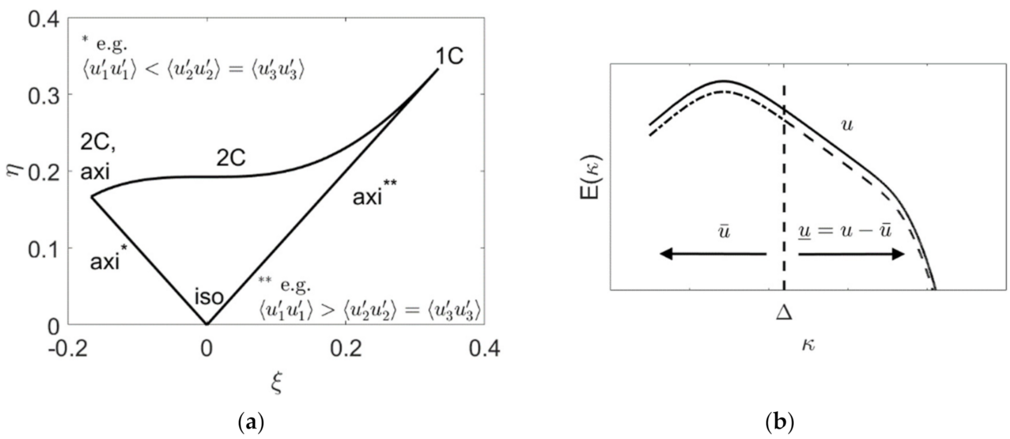

Figure 4. (**a**) Sketch of the Lumley triangle with its borders; (**b**) sketch of turbulence kinetic energy spectrum of velocity before (solid line), after applying a low pass filter which results in $\bar{u}$ (dash-dotted line) and after applying a high pass filter which results in $\underline{u}$ (dashed line). The axisymmetric contraction border (∗) signifies a situation where $\langle u_1'u_1'\rangle < \langle u_2'u_2'\rangle = \langle u_3'u_3'\rangle$, while the axisymmetric expansion (∗∗) signifies a situation where $\langle u_1'u_1'\rangle > \langle u_2'u_2'\rangle = \langle u_3'u_3'\rangle$.

For the purpose of this multiscale analysis, DNS data have been explicitly filtered by using a Gaussian filter kernel $G(r)$ such that the filtered values of a quantity Q can be expressed as follows.

$$\overline{Q(x)} = \int Q(x-r)G(r)dr,\ G(r) = \left(6/\pi\Delta^2\right)^{3/2}\exp\left(-6\,r\cdot r/\Delta^2\right) \quad (6)$$

The application of this low pass filter removes the high wavenumber content of the fluctuating velocity signal (refer to Figure 4b) and an associated high pass filter (which removes the low wavenumber content) can be defined by $\underline{Q} = Q - \overline{Q}$. In this paper, results will be presented from $\Delta/\delta_{th} = 0.4$, where the flame is partially resolved, up to $\Delta/\delta_{th} = 5.8$, where the flame becomes fully unresolved and Δ becomes larger than the integral length scale.

While the Reynolds stress tensor is usually defined as $T_{ij} = \langle u_i'u_j'\rangle$, Favre filtering is often applied in variable-density flows. The Favre-averaged Reynolds stress is defined as $T_{ij}^F = \langle\rho u_i''u_j''\rangle/\langle\rho\rangle$. Similarly, the Reynolds-averaged dissipation tensor can be defined as $\varepsilon_{ij} = 2\langle\nu\,\partial u_i'/\partial x_k\,\partial u_j'/\partial x_k\rangle$ or in the context of Favre averaging as $\varepsilon_{ij}^F = \langle t_{ij}s_{ij}''\rangle/\langle\rho\rangle$, where s_{ij}'' is the fluctuating strain tensor and $t_{ij} = 2\rho\nu s_{ij}'' - (2\rho\nu/3)\delta_{ij}s_{kk}''$ is the usual constitutive stress–strain relation [32]. Figure 5 shows that there is nearly no difference in the Lumley triangles of the Reynolds-averaged versus Favre-averaged Reynolds stress and dissipation tensors. Henceforth, the Favre-averaged version will be shown, and for the sake of simplicity, it will be denoted T_{ij} and ε_{ij}, respectively. Half the trace of T_{ij} (ε_{ij}) is usually referred to as turbulence kinetic energy k (dissipation of turbulence kinetic energy ε) [2].

In the context of LES, the unclosed term is called subgrid scale stress and is defined as $\tau_{ij} = \overline{u_i u_j} - \overline{u_i}\,\overline{u_j}$. Comparable to averaging, a Favre-filtered subgrid scale stress can be defined as $\tau^F_{ij} = \left(\overline{\rho u_i u_j} - \overline{\rho}\widetilde{u}_i\widetilde{u}_j\,\right)/\overline{\rho}$, where Favre-filtering is provided by $\widetilde{Q} = \overline{\rho Q}/\overline{\rho}$.

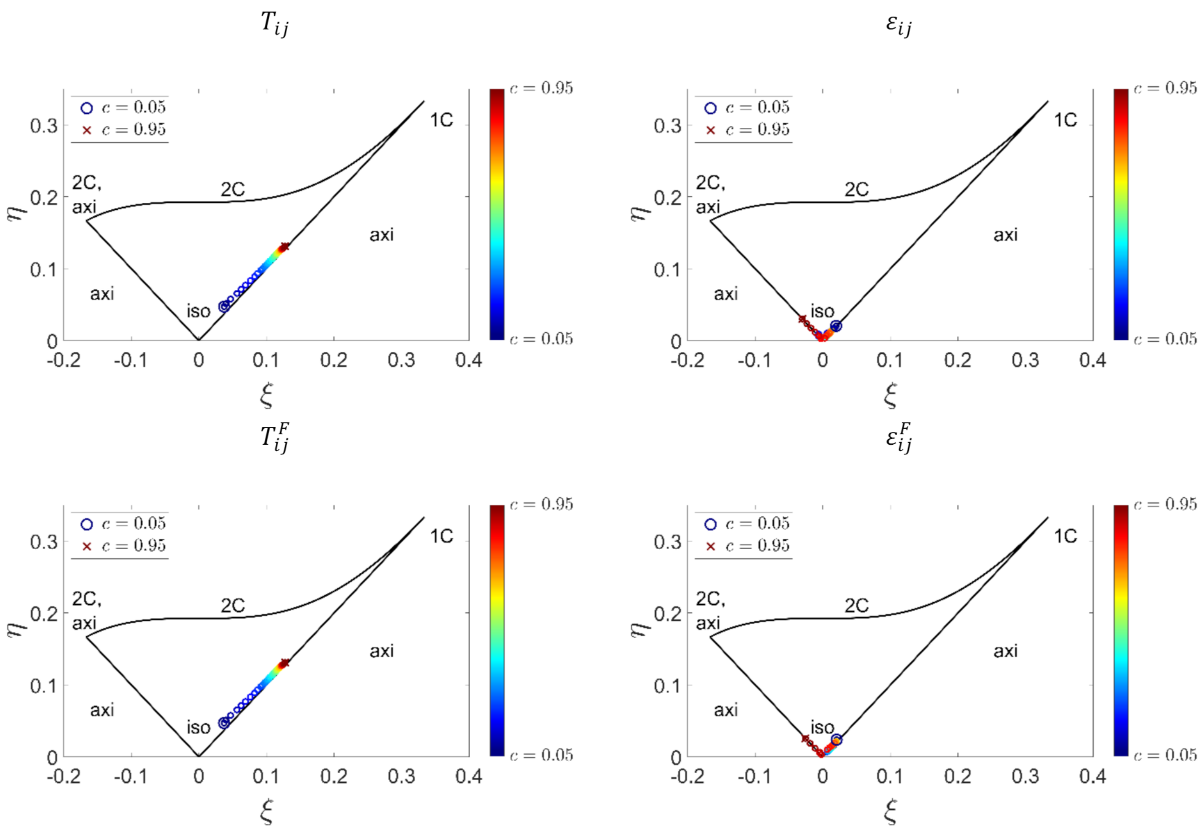

Figure 5. Anisotropies of the tensors T_{ij}, T^F_{ij}, ε_{ij} and ε^F_{ij} in the Lumley triangle shown exemplarily for case B. The left (right) column shows the turbulent state of the Reynolds stress (dissipation) tensor, while the first (second) row is related to Reynolds (Favre) averaging, respectively. The results are shown conditional on reaction progress variable c, as indicated by the colorbar. In addition, the first ($c = 0.05$) and last points ($c = 0.95$) are marked by a circle and a cross, respectively.

4. Results and Discussion

The distributions of k and ε in a x-y planes are shown in Figure 6. and it is obvious that their behaviour changes significantly from case A to case C. Turbulence kinetic energy and its dissipation can be scaled as $k \sim 1.5u'^2$ and $\varepsilon \sim k^{1.5}/l$, respectively [2]. According to Table 1 this suggests that, globally, k increases by a factor of about 56 and 225 from case A to B and case A to C, while dissipation increases by a factor of 422 and 3375, respectively. This explains the largely different scales in Figure 6. While case A shows indications of augmentations of k within the flame because of thermal expansion, turbulent velocity fluctuations decay from the unburned to the burned gas side for cases B and C due to the rise of kinematic viscosity. Furthermore, for case A, highest values of dissipation are obtained within the flame, but for cases B and C, the dissipation magnitude decreases from unburned gas to the burned gas side by roughly a factor 1/5.

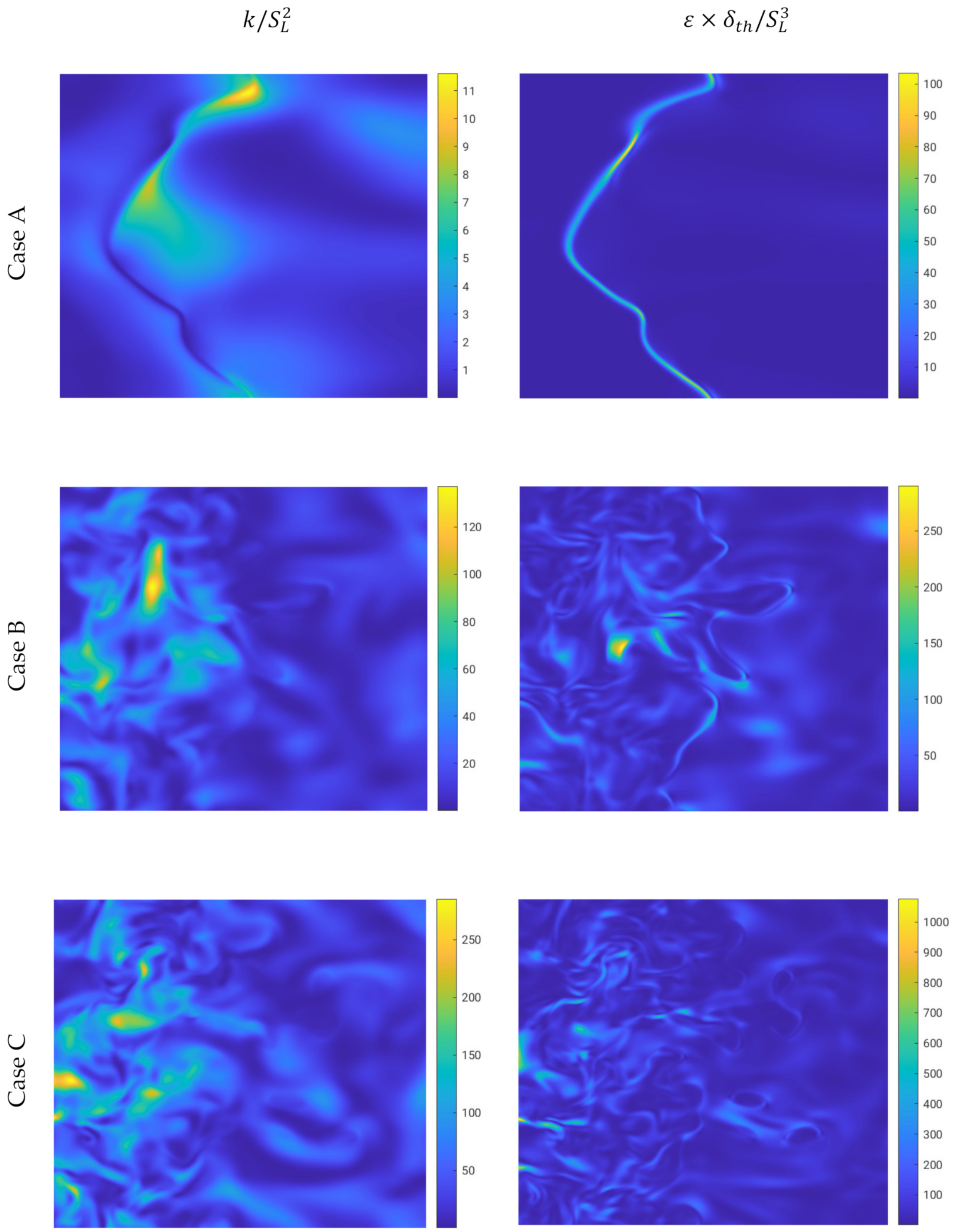

Figure 6. Instantaneous distribution of normalised turbulence kinetic energy (left) and normalised dissipation in the x-y plane for top-bottom cases A–C. The flame propagates from right to left along the negative x-direction. The field of view represents the computational domain of dimension $26.1\delta_{th} \times 26.1\delta_{th}$.

It can further be observed from Figure 6. that the dissipative structures are clearly smaller than the structures carrying turbulence kinetic energy, which is in agreement with the idea of scale separation between the scales injecting and dissipating energy (i.e., $l \gg \eta$ consistent with the scaling $l/\eta \sim Re_t^{3/4}$, see Table 1, where η denotes the Kolmogorov scale).

Multiscale [33,34] or spectral [35] analysis of turbulent premixed flames is frequently conducted in the homogeneous directions, because heat release does not allow a Fourier transform in the direction of mean flame propagation. It might be, therefore, of interest to study the effects of a 2D (i.e., in the y-z plane) versus a 3D Gaussian filter on flow anisotropies. The anisotropy of the tensor T_{ij} is shown in Figure 7 for cases A–C after the application of a high pass filter with $\Delta/\delta_{th} = 0.4$. By comparing the left and right columns, it can clearly be observed that results are qualitatively similar for both filters, but the anisotropies remain stronger in the case of 2D filtering because large structures in x-direction are not affected by filtering in the y-z plane. In the following, only results for the 3D filter will be shown. This does not impose any problems because the flames are sufficiently far away from the x-boundaries to allow for the application of the 3D filter.

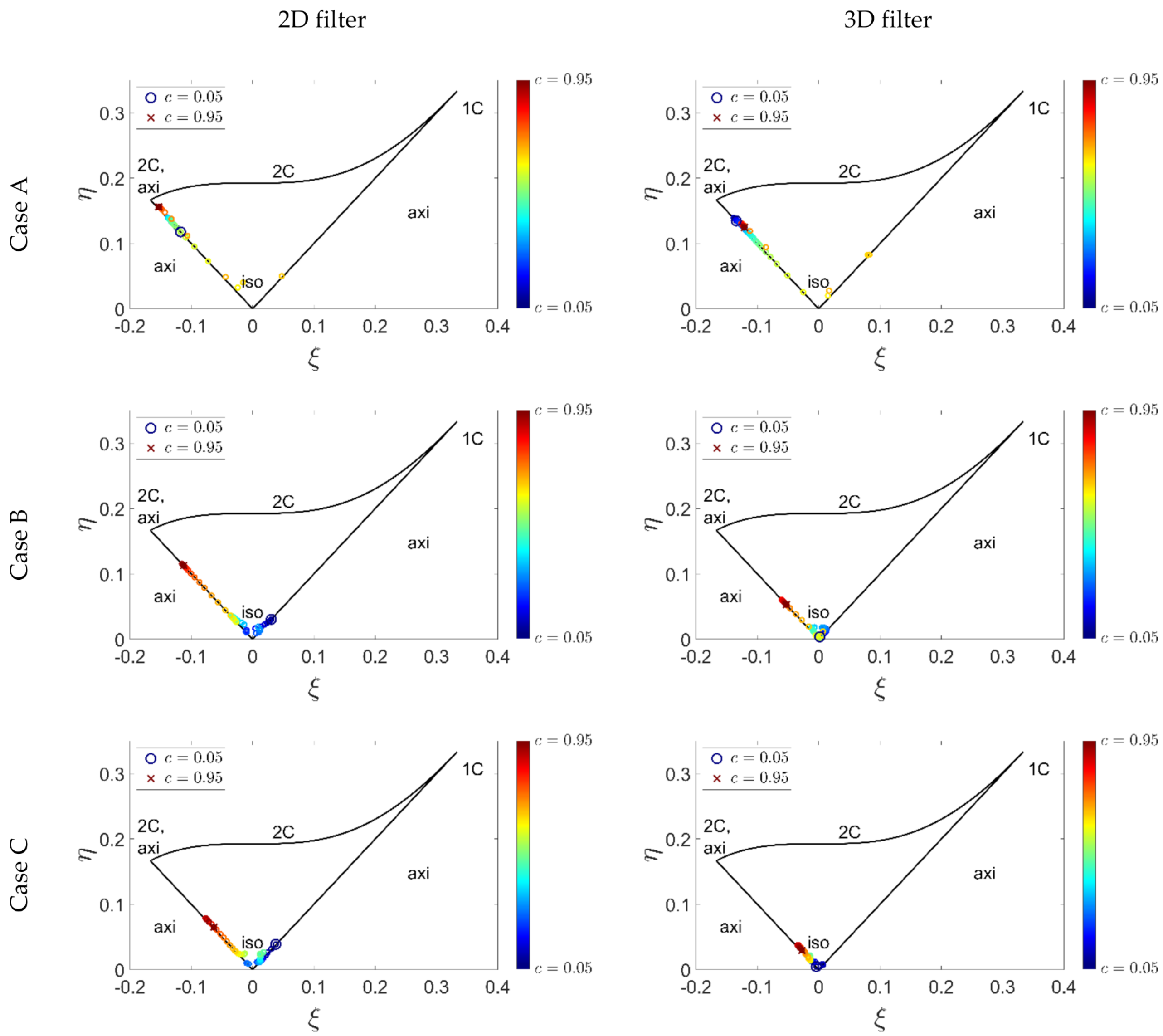

Figure 7. Anisotropy of the tensor T_{ij} in the Lumley triangle for cases A–C when applying a 2D versus a 3D Gaussian high pass filter with $\Delta/\delta_{th} = 0.4$. The results are shown to be conditional on reaction progress variable c, as indicated by the colorbar. In addition, the first (c = 0.05) and last points (c = 0.95) are marked by a circle and a cross, respectively.

In order to be able to correctly classify the following results for turbulent premixed flames, the anisotropies of the Reynolds stress and dissipation tensor from a channel flow simulation are exemplarily shown in Figure 8, where the data were taken from results presented in [36]. Data for the Reynolds stresses were shifted in vertical direction by 0.01 in order to be able to distinguish it from the dissipation data. Figure 8 shows that the anisotropies of T_{ij} and ε_{ij} are nearly identical, with only marginally more isotropy for ε_{ij} towards the channel center (indicated by the crosses). The same holds true for bubbly channel flow, as reported in [36], and the findings are also consistent with the early experimental data from turbulent boundary layers by Antonia et al. [4]: Very close to the wall in the viscous sublayer of the channel flow, the turbulence is essentially two-component, v being much smaller than u and w. Anisotropy reaches a peak at a dimensionless wall distance of about $y^+ = 7$ close to the 1C state and subsequently becomes increasingly isotropic towards the channel center [2]. Apart from the artificial offset, Figure 8 shows nearly the same behaviour for anisotropy based on Reynolds stress and dissipation tensors.

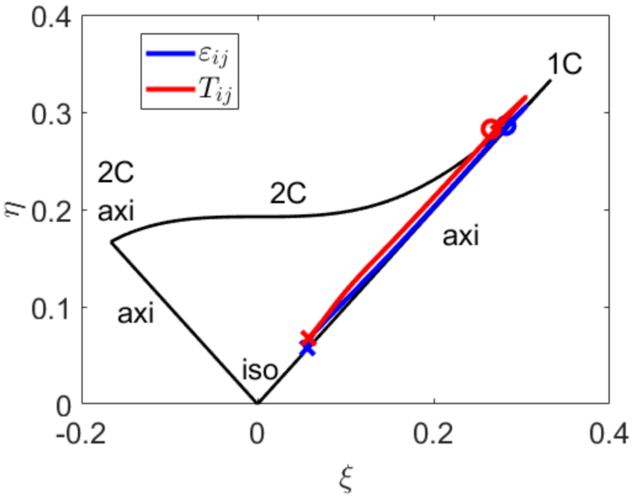

Figure 8. Anisotropy based on Reynolds stress and dissipation tensor for the channel flow data presented in [36]. The point closest to the wall is marked with a circle, whereas the channel center location is marked with a cross. Results for T_{ij} are shifted in direction of η by 0.01.

The results for the anisotropy of the tensors T_{ij} and ε_{ij} are shown in the Lumley triangle for cases A–C in Figures 9–11. The first row in each plot shows the results for unfiltered data, followed by the data after applying a high pass filter of sizes $\Delta/\delta_{th} = 5.8,\ 1.4,\ 0.4$, such that, for the last row, only the smallest structures remain. Focusing first on the unfiltered results in the first row of Figures 9–11, two things are apparent: (i) there is a pronounced anisotropy of the Reynolds stresses, particularly for case A, where thermal expansion effects dominate the turbulent velocity fluctuations. The turbulent state of the largest part of the statistically planar flame brush can be found on the axisymmetric expansion border which, for the flame propagation direction aligned with the x-direction, signifies a situation where $T_{11} > T_{22} = T_{33}$ (refer to Figure 4a). The initial background fluid motion is isotropic, and with increasing turbulence intensity (alternatively increasing Ka or decreasing Da, see Table 1), the relative contribution of thermal expansion effects weakens, and the flow fields becomes more isotropic. These observations are consistent with earlier findings in [15–17]: Turbulent premixed flames can cause strong anisotropies such that the turbulent state is located on the axisymmetric expansion border and reaches, for small turbulence intensities (e.g., $u'/S_L \approx 1$) from the isotropic state two-thirds up the way to one component's endpoint. For large turbulence intensities (e.g., $u'/S_L > 10$), a nearly isotropic behaviour can be observed: (ii) The dissipation tensor is considerably more isotropic than the Reynolds stress tensor but this difference decreases with decreasing Δ. For example, the maximum departure from the origin can reach up to $\xi = 0.27\ (0.13)$ and $\eta = 0.27\ (0.13)$ for T_{ij} in case A (case C), whereas the maximum departure from the origin extends to $\xi = 0.11\ (-0.024)$ and $\eta = 0.11\ (0.024)$ for ε_{ij} for the unfiltered condition. This situation changes to $\xi = -0.13\ (-0.028)$ and $\eta = 0.13\ (0.028)$ for T_{ij} in case A (case C), whereas the maximum departure from the origin extends to $\xi = -0.064$ (-0.03) and $\eta = 0.064$ (0.03) for ε_{ij} for $\Delta/\delta_{th} = 0.4$. The differences in anisotropy between T_{ij} and ε_{ij} tensors are in contrast to the observations from shear flows, as illustrated in Figure 8. Nevertheless, with increasing u'/S_L (which is equivalent to increasing Ka or decreasing Da for a given value of l/δ_{th}), isotropy increases (i.e., from case A to case C). This shows that linear relationships between the anisotropy of T_{ij} and ε_{ij} that might have been developed for shear flows are unlikely to work well for turbulent premixed flames. The effects of anisotropy on T_{ij} is dictated by the relative strengths of turbulent velocity fluctuation u' and the velocity jump due to thermal expansion, which can be characterised in terms of $NB \sim \tau S_L/u' \sim \tau/\left(Da^{1/2}Ka\right)$, whereas the anisotropy of ε_{ij} is dictated by the relative strengths of $a_{turb} \sim u'/l$ and $a_{chem} \sim \tau S_L/\delta_{th}$, which is dictated by τDa. This implies that a simple linear relationship between the anisotropy of T_{ij} and ε_{ij} is unlikely to be valid for premixed turbulent flames.

For a high pass filter of width Δ, flow structures smaller than Δ are retained such that the second, third and fourth row in Figures 9–11 represent increasingly small flow structures. For case C, the following behaviour is as expected: Both tensors T_{ij} and ε_{ij} tend to become more isotropic with decreasing filter width Δ. Isotropy, in particular, increases once the filter becomes smaller than the integral scale (i.e., $\Delta/\delta_{th} = 4.58$ according to Table 1). By contrast, case A shows an unexpected behaviour and the turbulent state switches from axisymmetric expansion (lower right border) to the axisymmetric contraction side (lower left border) with a decrease in Δ, but considerably anisotropy can be observed even for the smallest filter width considered here.

This unexpected behaviour warrants an explanation, which is provided in the following manner. The axisymmetric contraction signifies a situation where $T_{11} < T_{22} = T_{33}$ in the present scenario. This means that, for the smallest flow scales, the strong dilatation effects, responsible for the opposite scenario (i.e., $T_{11} > T_{22} = T_{33}$), are no longer present. This can be explained as follows. Figure 1 shows that flow structures corresponding to the fluctuating u velocity component are considerably larger compared to the v (or w, not shown) structures. By filtering the flow field with a filter width smaller than these, u velocity structures diminish their strength considerably until they finally vanish and only the smaller velocity fluctuations of the transverse components are left. Ultimately, this indicates that not only the fluctuation strength is anisotropic for case A but also the size of the structures associated with different velocity components is different. The behaviour of Case B is somewhere in between case A and case C. It is worth remarking that the value of k decreased by roughly 50% at the time statistics were taken. As a result, Bray number $NB \sim \tau S_L/u'$ for case B increases from 0.6 to a value close to unity. This also implies that the Damköhler (Karlovitz) number Da (Ka) increases (decreases) roughly by a factor of 1.414 (0.6) in comparison to the initial values in case B.

Finally, the anisotropy of the subgrid scale stress tensor is analysed in Figure 12 for filter widths $\Delta/\delta_{th} = 0.4,\ 1.4, 5.8$ and 11.6. In contrast to the previous results, a low pass filter is used in this context and the unfiltered result (which would result in a vanishing subgrid scale contribution) has been replaced with an even larger filter width of $\Delta/\delta_{th} = 11.6$. Only cases A and B are shown in Figure 12 because the subgrid scale stresses for case C are nearly isotropic even for the largest filter width. Figure 12 shows that the subgrid scale stresses are considerably more isotropic than their averaged counterparts, and this statement holds for the entire range of filter width. Again, isotropy increases with increasing u'/S_L, qualitatively similar to the Reynolds/Favre-averaged equivalents. The same physical explanations which were mentioned earlier in the context of RANS to explain the greater extent of isotropy for T_{ij} and ε_{ij} for the cases with high turbulence intensities are also qualitatively valid in the context of subgrid quantities.

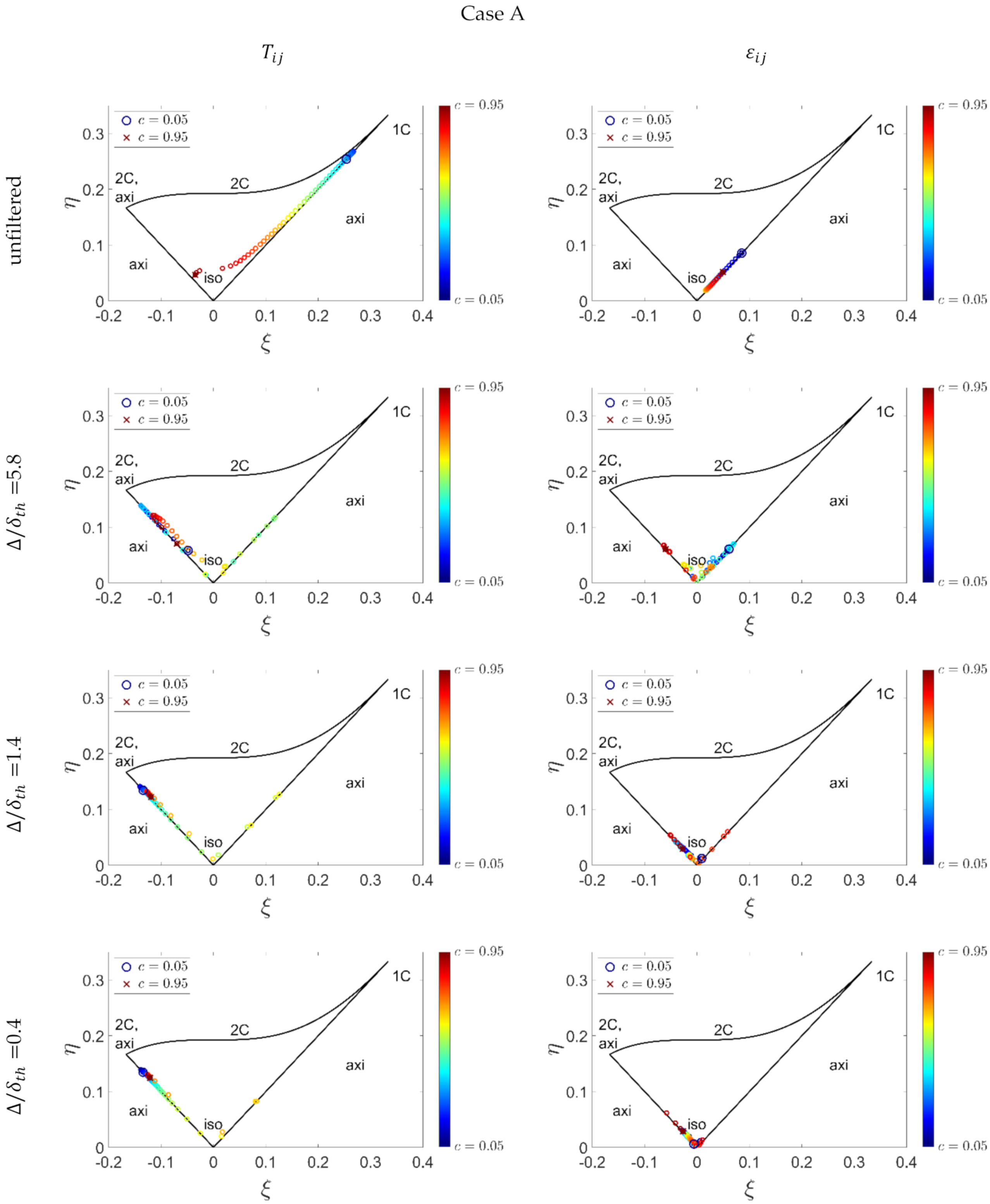

Figure 9. Anisotropy of the tensors T_{ij} and ε_{ij} shown in the Lumley triangle for case A. A Gaussian high pass filter with (bottom to top) $\Delta/\delta_{th} = 0.4,\ 1.4$ and 5.8 is used and compared to the results from the unfiltered data. The results are shown conditional on reaction progress variable c, as indicated by the colorbar. In addition, the first (c = 0.05) and last points (c = 0.95) are marked by a circle and a cross, respectively.

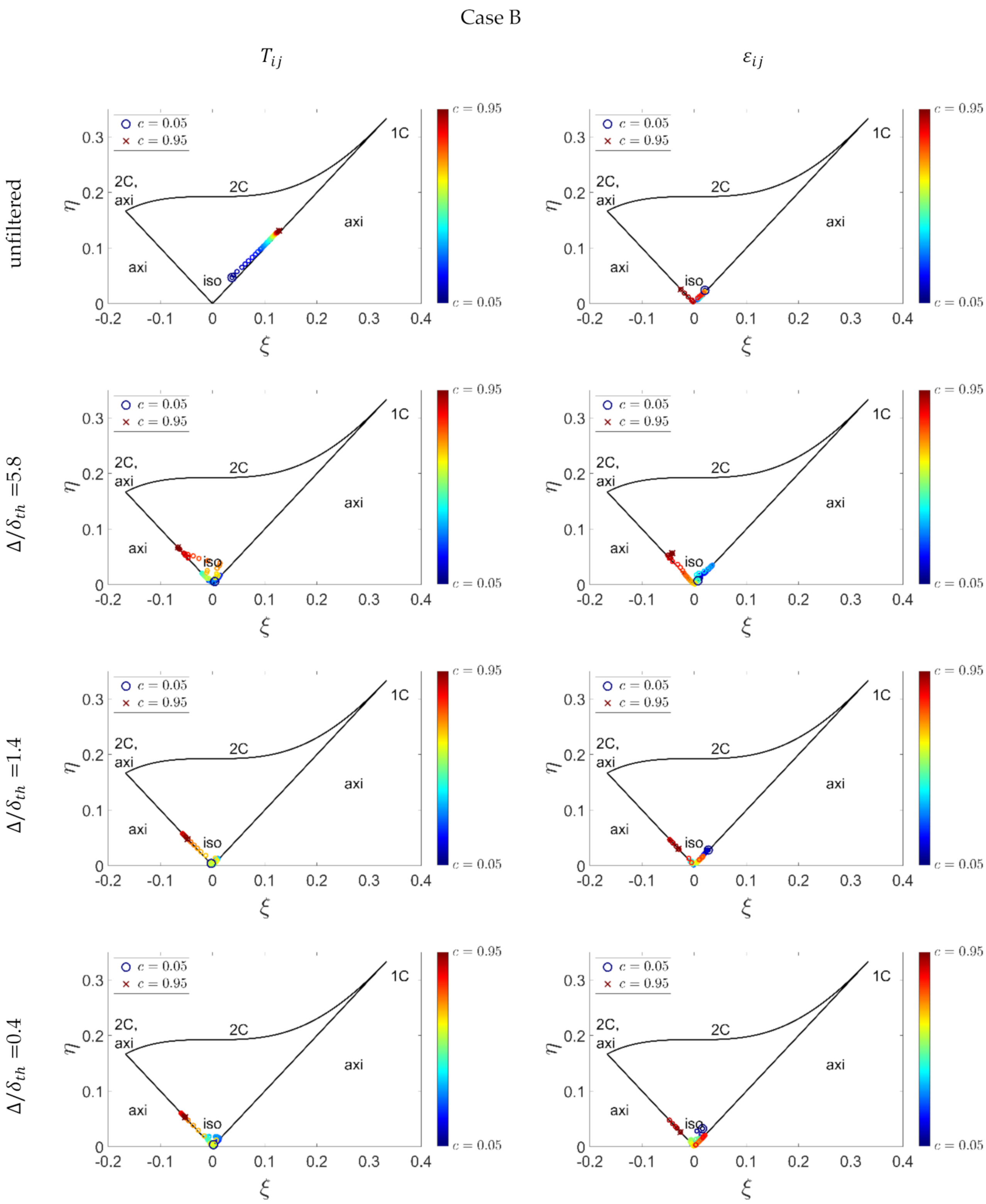

Figure 10. Anisotropy of the tensors T_{ij} and ε_{ij} shown in the Lumley triangle for case B. A Gaussian high pass filter with (bottom to top) $\Delta/\delta_{th} = 0.4,\ 1.4$ and 5.8 is used and compared to the results from unfiltered data. The results are shown conditional on reaction progress variable c, as indicated by the colorbar. In addition, the first (c = 0.05) and last points (c = 0.95) are marked by a circle and a cross, respectively.

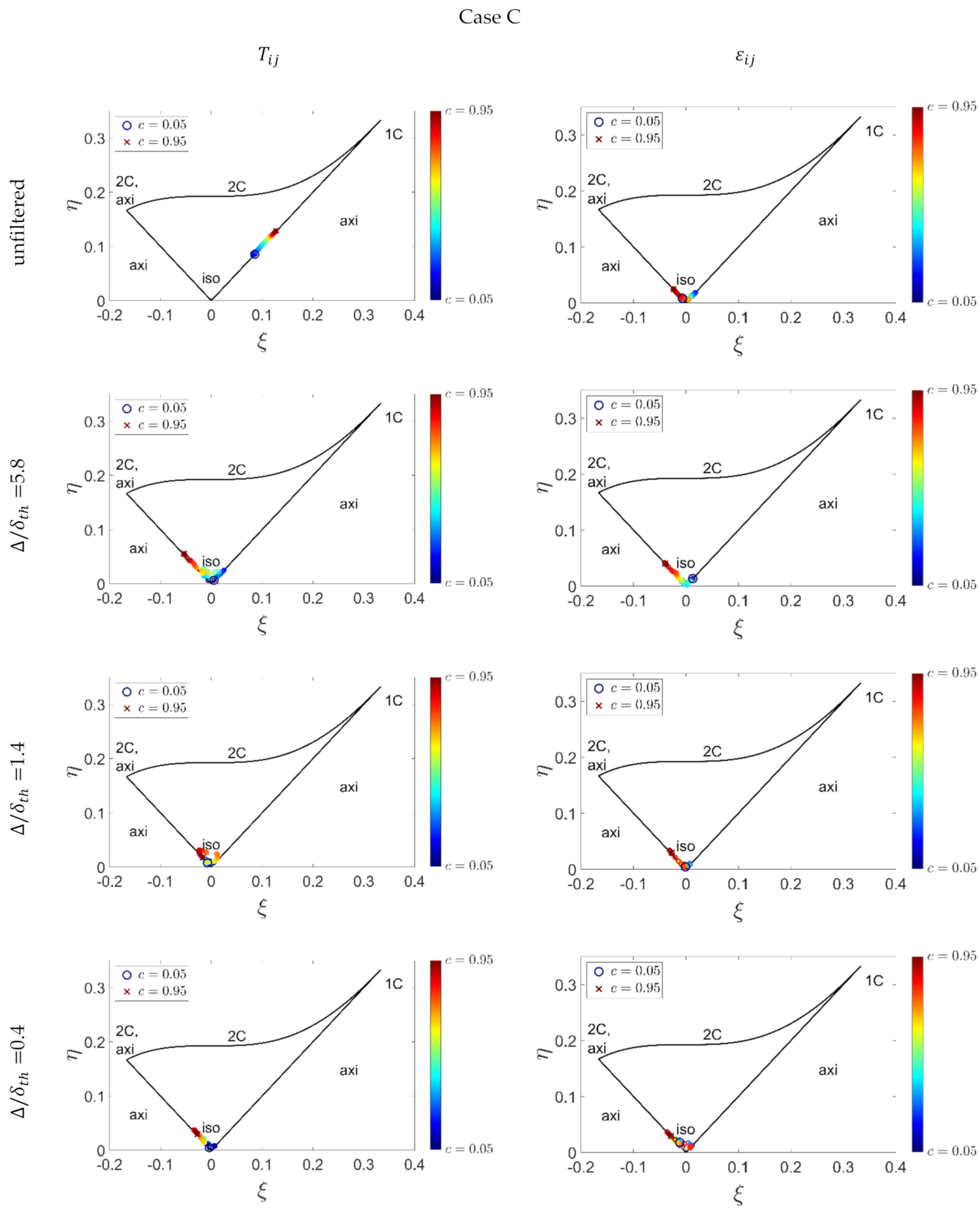

Figure 11. Anisotropy of the tensors T_{ij} and ε_{ij} shown in the Lumley triangle for case C. A Gaussian high pass filter with (bottom to top) $\Delta/\delta_{th} = 0.4$, 1.4 and 5.8 is used and compared to the results from unfiltered data. The results are shown conditional on reaction progress variable c, as indicated by the colorbar. In addition, the first (c = 0.05) and last points (c = 0.95) are marked by a circle and a cross, respectively.

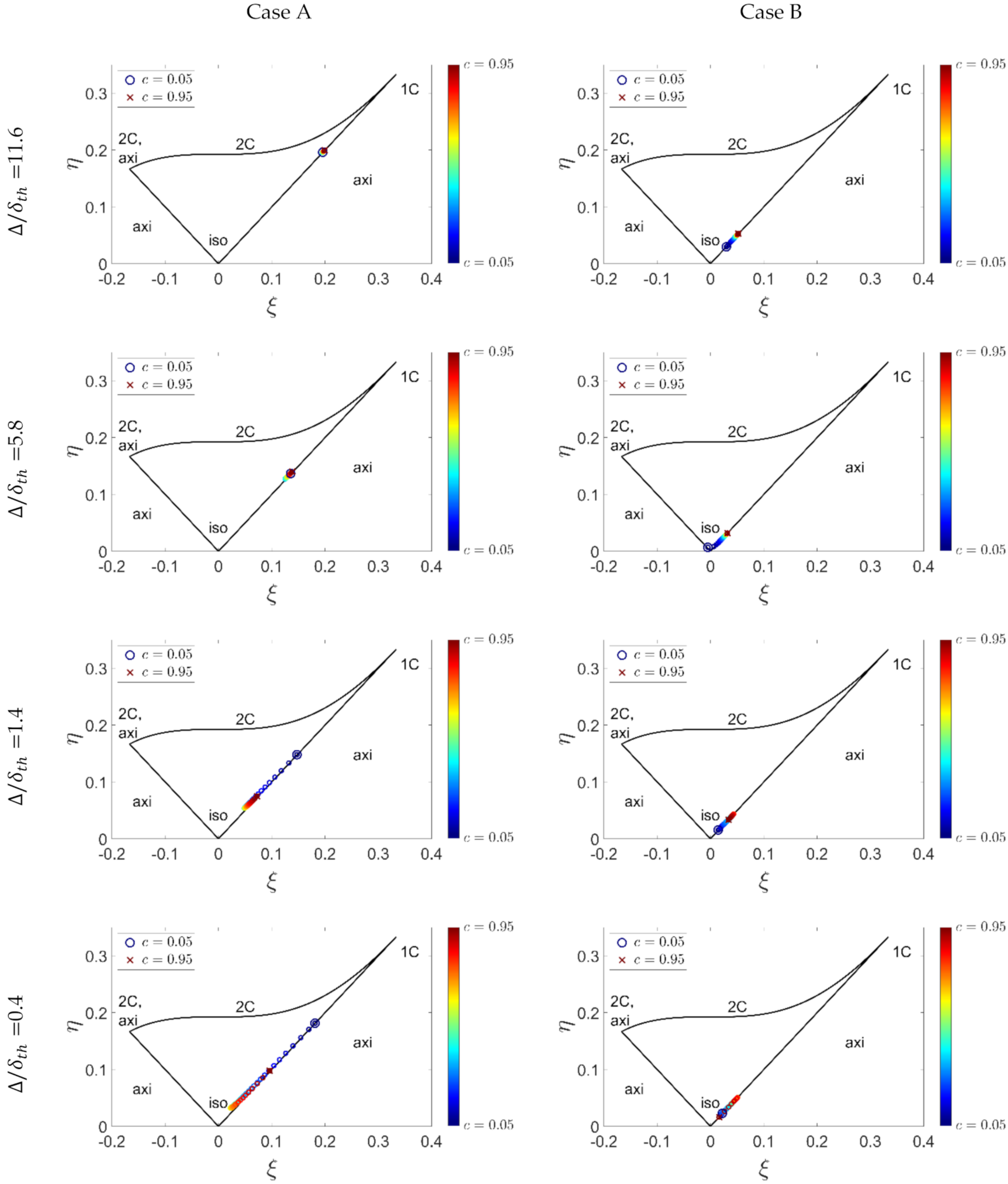

Figure 12. Anisotropy of the subgrid scale tensors τ_{ij} shown in the Lumley triangle for cases A and B. A Gaussian low pass filter with (bottom to top) $\Delta/\delta_{th} = 0.4,\ 1.4, 5.8$ and 11.6 is used. The results are shown conditional on reaction progress variable c, as indicated by the colorbar. In addition, the first (c = 0.05) and last points (c = 0.95) are marked by a circle and a cross, respectively.

The modification of anisotropy distribution in the Lumley triangle in turbulent premixed flames in comparison to that in the corresponding non-reacting flow has been reported in [15], and these findings have, in the meantime, been confirmed independently by a few other DNS groups [37–39]: Turbulent premixed flames cause strong anisotropies such that the turbulent state is located on the axisymmetric expansion border and reaches, depending on the turbulence intensity (Karlovitz number), from the isotropic state two-thirds up the way to the one component endpoint. Furthermore, early measurements of the enhancement of turbulence anisotropy in large-scale, low-intensity turbulent premixed propane-air flames using two-component measurements have been reported by Furukuwa et al. [40].

It has been shown in the past [15,16,41] that the phenomenon of counter-gradient transport or counter-gradient stresses, as theoretically predicted by Bray and co-workers [28], is closely related to the axisymmetric expansion turbulent state. Its existence in the context of LES has been confirmed by very recent and advanced measurement techniques [42] that result in the conclusion that LES models should allow for upscale energy transfer in the vicinity of the flame. In addition, in the context of unsteady RANS or hybrid RANS/LES, the present results suggest the invalidity of the Boussinesq assumption and the need for an anisotropic correction, which will depend on how much of the turbulence kinetic energy can be resolved, as revealed by the multiscale analysis.

While the aforementioned findings can be considered an indirect or partial validation of the present results (at least for the case when the velocity field is not filtered), future analysis will be needed to confirm the present findings experimentally and by independent simulation groups including other configurations and different combustion regimes. This includes, in particular, the need for further multiscale analysis, which so far cannot be found in the open literature neither from experiment nor from simulation.

5. Conclusions

The anisotropy of the Reynolds stress, dissipation, and subgrid scale tensor in turbulent premixed flames with a range of different turbulence intensities has been characterised using the Lumley triangle by performing a multiscale analysis. For this purpose, an existing DNS database of statistically planar turbulent premixed flames has been filtered for a large range of filter widths ranging from dimensions smaller than the thermal flame thickness to structures that are larger than the integral scale. The main findings, which are reported for the first time for turbulent premixed flames, can be summarised as follows:

(i) Although the initial background fluid motion is isotropic, there is a pronounced anisotropy towards the axisymmetric expansion for low turbulence intensities. This effect diminishes with increasing turbulence intensity.

(ii) In general, this anisotropy decreases with decreasing high pass filter width (i.e., when only smaller and smaller structures remain), but for case A (i.e., the case with the smallest value of u'/S_L), the state of the turbulent flow flips towards the axisymmetric contraction side. This trend has been explained by the different size of flow structures associated with velocity components in the direction of mean flame propagation and transverse to it.

(iii) The dissipation tensor tends to be more isotropic than the Reynolds stress tensor, which is in agreement with the theoretical expectation. The behaviour is different to the turbulent boundary layers, where a much closer coupling can be observed.

(vi) In agreement with theoretical arguments, subgrid scale stresses are more isotropic than their averaged counterparts for all filter widths. Nevertheless, the axisymmetric expansion state is observed for low turbulence intensities.

(v) No remarkable differences were observed when using Reynolds averaging versus Favre averaging procedures and definitions.

(vi) The application of a 2D (in direction perpendicular to flame propagation) filter results qualitatively in very similar outcomes but the anisotropies remain stronger. While the pronounced anisotropy towards axisymmetric expansion for low turbulence intensities has been observed in earlier work for Reynolds stresses [15–17], the present analysis confirms this trend for the dissipation tensor and further extends the findings to a multiscale analysis and shows several unexpected (e.g., the flipping of the turbulent state mentioned in (ii)) and interesting aspects (e.g., no difference between Reynolds and Favre-Averaging based definitions (v), or the quantification of 2D vs.

3D filtering (vi)). However, the analysis is limited to moderate Reynolds numbers, and more analysis will be needed in future to observe if the above trends persist at higher Reynolds numbers.

Author Contributions: Conceptualization, M.K. and N.C.; methodology, M.K.; software, N.U. and T.T.; formal analysis, N.U.; resources, M.K.; writing—original draft preparation, M.K. and N.C.; writing—review and editing, M.K. and N.C.; visualization, N.U. and M.K. supervision, T.T. and M.K. All authors have read and agreed to the published version of the manuscript.

Funding: Funding by dtec.bw—Digitalization and Technology Research Center of the Bundeswehr, Project MORE—is gratefully acknowledged. NC acknowledges Engineering and Physical Sciences Research Council (EP/R029369/1) for financial and computational support.

Institutional Review Board Statement: Not applicable.

Informed Consent Statement: Not applicable.

Data Availability Statement: The data that support the findings of this study are available from the corresponding author upon reasonable request.

Conflicts of Interest: The authors declare no conflict of interest.

References

1. Kolmogorov, A.N. Local Structure of Turbulence in an Incompressible Fluid at Very High Reynolds Numbers. *Dokl. Akad. Nauk SSSR* **1941**, *30*, 299–303. [CrossRef]
2. Pope, S.B. *Turbulent Flows*; Cambridge University Press: Cambridge, UK, 2000.
3. Hanjalić, K.; Launder, B.E. Contribution towards a Reynolds-stress closure for low-Reynolds-number turbulence. *J. Fluid Mech.* **1976**, *74*, 593–610. [CrossRef]
4. Antonia, R.A.; Djenidi, L.; Spalart, P.R. Anisotropy of the dissipation tensor in a turbulent boundary layer. *Phys. Fluids* **1994**, *6*, 2475–2479. [CrossRef]
5. Liu, K.; Pletcher, R.H. Anisotropy of a turbulent boundary layer. *J. Turbul.* **2008**, *9*, N18. [CrossRef]
6. Launder, B.E. Second-moment closure: Present and future? *Int. J. Heat Fluid Flow* **1989**, *10*, 282–300. [CrossRef]
7. Speziale, C.G. Analytical Methods for the Development of Reynolds-Stress Closures in Turbulence. *Ann. Rev. Fluid Mech.* **1991**, *23*, 107–157. [CrossRef]
8. Hanjalić, K.; Brian Launder, B. *Modelling Turbulence in Engineering and the Environment: Second-Moment Routes to Closure*; Cambridge University Press: Cambridge, UK, 2011.
9. Leschziner, M. *Statistical Turbulence Modelling for Fluid Dynamics—Demystified: An Introductory Text for Graduate Engineering Students*; Imperial Coll. Press: London, UK, 2016.
10. Durbin, P.A.; Reif, B.A.P. *Statistical Theory and Modeling for Turbulent Flows*, 2nd ed.; Wiley: New York, NY, USA, 2010. [CrossRef]
11. Sreenivasan, K.R.; Antonia, R.A. The phenomology of small-scale turbulence. *Ann. Rev. Fluid Mech.* **1997**, *29*, 435–472. [CrossRef]
12. Shen, X.; Warhaft, Z. The anisotropy of the small scale structure in high Reynolds number (Reλ~1000) turbulent shear flow. *Phys. Fluids* **2000**, *12*, 2976–2989. [CrossRef]
13. Clavin, P.; Williams, F.A. Theory of premixed-flame propagation in large-scale turbulence. *J. Fluid Mech.* **1979**, *90*, 589–604. [CrossRef]
14. Libby, P.A.; Bray, K. Countergradient Diffusion in Premixed Turbulent Flames. *AIAA J.* **1981**, *19*, 205–213. [CrossRef]
15. Klein, M.; Kasten, C.; Chakraborty, N. A-priori Direct Numerical Simulation assessment of models for generalized sub-grid scale turbulent kinetic energy in turbulent premixed flames. *Comput. Fluids* **2017**, *154*, 123–131. [CrossRef]
16. Klein, M.; Kasten, C.; Chakraborty, N.; Mukhadiyev, N.; Im, H.G. Turbulent scalar fluxes in H2-air premixed flames at low and high Karlovitz numbers. *Combust. Theory Model.* **2018**, *22*, 1033–1048. [CrossRef]
17. Brearley, P.; Ahmed, U.; Chakraborty, N.; Klein, M. Scaling of Second-Order Structure Functions in Turbulent Premixed Flames in the Flamelet Combustion Regime. *Fluids* **2020**, *5*, 89. [CrossRef]
18. Lumley, J. Computational Modeling of Turbulent Flows. *Adv. Appl. Mech.* **1979**, *18*, 123–176.
19. Klein, M.; Chakraborty, N. A-priori analysis of an alternative wrinkling factor definition for flame surface density based Large Eddy Simulation modelling of turbulent premixed combustion. *Combust. Sci. Technol.* **2018**, *191*, 95–108. [CrossRef]
20. Keil, F.B.; Klein, M.; Chakraborty, N. Sub-grid Reaction Progress Variable Variance Closure in Turbulent Premixed Flames. *Flow Turbul. Combust.* **2020**, *106*, 1195–1212. [CrossRef]
21. Rasool, R.; Chakraborty, N.; Klein, M. Effect of non-ambient pressure conditions and Lewis number variation on direct nu-merical simulation of turbulent Bunsen flames at low turbulence intensity. *Combust. Flame* **2021**, *231*, 111500. [CrossRef]
22. Jenkins, K.W.; Cant, R.S. Direct Numerical Simulations of turbulent flame kernels. In *Recent Advances in DNS and LES*; Springer: New York, NY, USA, 1999; pp. 191–202.

23. Keil, F.B.; Amzehnhoff, M.; Ahmed, U.; Chakraborty, N.; Klein, M. Comparison of Flame Propagation Statistics Extracted from Direct Numerical Simulation Based on Simple and Detailed Chemistry—Part 1: Fundamental Flame Turbulence Interaction. *Energies* **2021**, *14*, 5548. [CrossRef]
24. Klein, M.; Chakraborty, N.; Ketterl, S. A Comparison of Strategies for Direct Numerical Simulation of Turbulence Chemistry Interaction in Generic Planar Turbulent Premixed Flames. *Flow, Turbul. Combust.* **2017**, *99*, 955–971. [CrossRef]
25. Ahmed, U.; Herbert, A.; Chakraborty, N.; Klein, M. On the validity of Damköhler's second hypothesis in statistically planar turbulent premixed flames in the thin reaction zones regime. *Proc. Combust. Inst.* **2020**, *38*, 3039–3047. [CrossRef]
26. Jacobs, C.T.; Jammy, S.P.; Sandham, N.D. OpenSBLI: A framework for the automated derivation and parallel execution of finite difference solvers on a range of computerarchitectures. *J. Comput. Sci.* **2017**, *18*, 12–33. [CrossRef]
27. Wang, Z.J.; Fidkowski, K.; Abgrall, R.; Bassi, F.; Caraeni, D.; Cary, A.; Deconinck, H.; Hartmann, R.; Hillewaert, K.; Huynh, H.T. High-order CFD methods: Current status and perspective. *Int. J. Numer. Meth. Fluids* **2013**, *72*, 811–845. [CrossRef]
28. Bray, K.; Libby, P.A.; Moss, J. Unified modeling approach for premixed turbulent combustion—Part I: General formulation. *Combust. Flame* **1985**, *61*, 87–102. [CrossRef]
29. Veynante, D.; Trouvé, A.; Bray, K.N.C.; Mantel, T. Gradient and counter-gradient scalar transport in turbulent premixed flames. *J. Fluid Mech.* **1997**, *332*, 263–293. [CrossRef]
30. Tennekes, H.; Lumley, J.L. *A First Course in Turbulence*, 1st ed.; MIT Press: Cambridge, MA, USA, 1992; ISBN 978-0-262-20019-6.
31. Chakraborty, N.; Swaminathan, N. Influence of Damköhler number on turbulence-scalar interaction in premixed flames. *Part I Phys. Insight Phys. Fluids* **2007**, *19*, 045103.
32. Wilcox, D.C. *Turbulence Modelling for CFD*; DCW Industries: La Canada, CA, USA, 1998.
33. Ahmed, U.; Doan, N.A.K.; Lai, J.; Klein, M.; Chakraborty, N.; Swaminathan, N. Multiscale analysis of head-on quenching premixed turbulent flames. *Phys. Fluids* **2018**, *30*, 105102. [CrossRef]
34. Doan, N.; Swaminathan, N.; Chakraborty, N. Multiscale analysis of turbulence-flame interaction in premixed flames. *Proc. Combust. Inst.* **2016**, *36*, 1929–1935. [CrossRef]
35. Kolla, H.; Hawkes, E.R.; Kerstein, A.R.; Swaminathan, N.; Chen, J.H. On velocity and reactive scalar spectra in turbulent premixed flames. *J. Fluid Mech.* **2014**, *754*, 456–487. [CrossRef]
36. Trautner, E.; Klein, M.; Bräuer, F.; Hasslberger, J. Conditional and unconditional second-order structure functions in bubbly channel flows of power-law fluids. *Phys. Fluids* **2021**, *33*, 055121. [CrossRef]
37. You, J.; Lu, Z.; Yang, Y. Anisotropic velocity statistics and vortex surfaces in turbulent premixed combustion. *Actca Aero-Dyn. Sin.* **2020**, *38*, 603–610.
38. Zhao, S.; Er-raiy, A.; Bouali, Z.; Mura, A. Dynamics and kinematics of the reactive scalar gradient in weakly turbulent premixed flames. *Combust. Flame* **2018**, *198*, 436–454. [CrossRef]
39. MacArt, J.F.; Grenga, T.; Mueller, M.E. Effects of combustion heat release on velocity and scalar statistics in turbulent premixed jet flames at low and high Karlovitz numbers. *Combust. Flame* **2018**, *191*, 468–485. [CrossRef]
40. Furukawa, J.; Noguchi, Y.; Hirano, T.; Williams, F.A. Anisotropic enhancement of turbulence in large-scale, low-intensity turbulent premixed propane–air flames. *J. Fluid Mech.* **2002**, *462*, 209–243. [CrossRef]
41. Klein, M.; Kasten, C.; Gao, Y.; Chakraborty, N. A-priori direct numerical simulation assessment of sub-grid scale stress tensor closures for turbulent premixed combustion. *Comput. Fluids* **2015**, *122*, 1–11. [CrossRef]
42. Kazbekov, A.; Steinberg, A.M. Physical space analysis of cross-scale turbulent kinetic energy transfer in premixed swirl flames. *Combust. Flame* **2021**, *229*, 111403. [CrossRef]